Research Article | Vol. 12, No. 12 / 1 Dec 2021 / Biomedical Optics Express 7918
Biomedical Optics EXPRESS

Intravital two-photon imaging and quantification of hepatic steatosis and fibrosis in a live small animal model

JIEUN MOON,[1,2] JEHWI JEON,[2,3] EUNJI KONG,[2,3] SUJUNG HONG,[1,2] JINGU LEE,[1,2] EUN KYUNG LEE,[4] AND PILHAN KIM[1,2,3,*]

[1]Graduate School of Nanoscience and Technology, Korea Advanced Institute of Science and Technology (KAIST), 291 Daehak-ro, Yuseong-gu, Daejeon, 34141, Republic of Korea
[2]KI for Health Science and Technology (KIHST), Korea Advanced Institute of Science and Technology (KAIST), 291 Daehak-ro, Yuseong-gu, Daejeon, 34141, Republic of Korea
[3]Graduate School of Medical Science and Engineering, Korea Advanced Institute of Science and Technology (KAIST), 291 Deahak-ro, Yuseong-gu, Daejeon, 34141, Republic of Korea
[4]Department of Internal Medicine, National Cancer Center, Goyang, 10408, Republic of Korea
*pilhan.kim@kaist.ac.kr

Abstract: Nonalcoholic fatty liver disease (NAFLD) is one of the most common chronic liver diseases closely associated with the metabolic system, including obesity and type 2 diabetes. The progression of NAFLD with advanced fibrosis is associated with an increased risk of liver cirrhosis and cancer as well as various extra-hepatic diseases. Yet, the underlying mechanism is not fully understood partly due to the absence of effective high-resolution *in vivo* imaging methods and the appropriate animal models recapitulating the pathology of NAFLD. To improve our understanding about complex pathophysiology of NAFLD, the need for an advanced imaging methodology to visualize and quantify subcellular-level features of NAFLD *in vivo* over time is ever-increasing. In this study, we established an advanced *in vivo* two-photon imaging technique to visualize and quantify subcellular-level pathological features of NAFLD in a live mouse animal developing hepatic steatosis, fibrosis, and disrupted microvasculature.

1. Introduction

Nonalcoholic fatty liver disease (NAFLD), a disease entity characterized by the accumulation of triglycerides within hepatocytes, is one of the most common chronic liver diseases in the world [1,2]. The underlying mechanism of this accumulation is not fully understood, but strongly associated with metabolic syndrome consisting of obesity [3] and type 2 diabetes [4]. NAFLD progression with the development of advanced fibrosis is associated with increased risk of liver cirrhosis and cancer as well as extra-hepatic diseases such as cardiovascular diseases and mortality [5,6]. The gold standard for diagnosing NAFLD is liver biopsy [7,8] despite potential complications such as bleeding and pain. Recent guidelines have recommended alternative magnetic resonance imaging or ultrasound scanning [9], though they are not capable of quantitative cellular-level assessment of NAFLD. For large-scale screening test, scoring systems derived from serum biomarkers are preferred due to the accessibility and additional cost of imaging studies [10,11]. Nevertheless, unfortunately, their performance does not reach the accuracy of liver biopsy.

To improve our understanding about complex pathophysiology of NAFLD, needs for an advanced imaging methodology to visualize and quantify subcellular-level features of NAFLD is ever-increasing. Intravital two-photon microscopy has been recognized as an advanced *in vivo* high-resolution imaging method to visualize dynamic biological phenomena in various tissues of live animal model [12,13]. Especially, two-photon excitation fluorescence (TPEF) and second harmonic generation (SHG) imaging can enable an *in vivo* visualization of collagen [14] and

#442608 https://doi.org/10.1364/BOE.442608
Journal © 2021 Received 6 Sep 2021; revised 24 Oct 2021; accepted 16 Nov 2021; published 1 Dec 2021

Biomedical Optics EXPRESS

subcellular compartments in microscopic resolution comparable to conventional histological observation of harvested *ex vivo* tissue.

Herein, we achieved an *in vivo* 3D subcellular-level visualization of hepatocellular steatosis and fibrosis in the liver of streptozotocin (STZ)-treated high-fat diet (HFD) fed mice using a custom-built intravital two-photon microscope. To fully induce hepatic steatosis with advanced fibrosis, a chronic condition with the result of long-term liver injury due to inflammation and microenvironmental stress including metabolic stress by excessive fat, the mice were fed the high-fat diet for 27 weeks [15–17]. Histologic hallmarks of NAFLD [18,19], the accumulation of hepatic lipid droplets (LDs) in hepatocytes, collagen fibers in perisinusoidal region, and the disruption of microvasculature were clearly visualized in subcellular level and quantified *in vivo*.

2. Methods

2.1. Animal model

All mice were maintained in independently ventilated, temperature & humidity-controlled cages (22.5 °C, 52.5%) under 12:12 hours light:dark cycle and provided with standard diet and water ad libitum. Insulin deficiency was induced in male C57BL/6 mice (OrientBio, Korea) by a single high dose (150 mg/kg body weight in 0.1M citrate buffer) intraperitoneal injection of streptozotocin (S0130, Sigma) at 6 weeks of age. One week later after the STZ injection, mice were fed with high-fat diet (Envigo, USA) for 27 weeks. As a control, mice received intraperitoneal injection of equal volume of 0.1M citrate buffer (C0759, Sigma) were fed with normal diet for the same period. STZ injection-induced hyperglycemia was monitored by measuring a fasting blood glucose level after 8hr fasting. Statistically significant increases in the fasting blood glucose (>300 mg/dL, hyperglycemia) and weight gain in STZ-treated high-fat diet mice compared to non-diabetic control mice were confirmed. All animal experiments were performed in accordance with the health guidelines for the use of experimental animals and were approved by the Institutional Animal Care and Use Committee (IACUC) of Korea Advanced Institute of Science and Technology (protocol no. KA-2018-78). All surgical procedures were performed under anesthesia, and all efforts were made to minimize the suffering of the animals.

2.2. Imaging system

A previously described custom-built laser-scanning two-photon microscopy system was used [20]. A tunable fs-pulse Ti:Sapphire laser (Chameleon Vison S, Coherent, USA) was used as a laser source for two-photon excitation. Half-wave plate combined with polarizer were used to control the laser intensity. Raster-pattern laser-scanning was achieved by using a rotating polygonal mirror (MC-5, Lincoln Laser, Canada) for x-axis scanning and a galvanomirror (6230H, Cambridge Technology, USA) for y-axis scanning as previously described [21–26]. The scanning laser beam was delivered to the liver of anesthetized mouse through commercial high numerical aperture objective lens (CFI75ApoLWD25XW, NA 1.1, Nikon, Japan). Fluorescence signals were collected by the objective lens in epi-detection manner and reflected by dichroic beam splitters (DBS1; FF705-Di01, Semrock, USA) toward fluorescence detectors (PMT: photomultiplier tube, R7518, Hamamatsu, Japan). Shortpass filter (SPF; FF720/SP, Semrock, USA) was used to block the excitation fs-pulse laser. For simultaneous multi-color imaging, the collected fluorescence signals were further spectrally separated by dichroic beam splitters (DBS2; FF495-Di03, DBS3; FF555-Di02, Semrock, USA) and then filtered by bandpass filters (BPF1; FF01-445/20, BPF2; FF01-525/45, BPF3; FF01-585/40, Semrock, USA). Electronic signals from the PMTs were acquired by using multi-channel frame grabber (Solios, Matrox, Canada) with a custom-written software based on Matrox Imaging Library (MIL10, Matrox, Canada).

Biomedical Optics EXPRESS

2.3. Intravital liver imaging

Mice were anesthetized with intraperitoneal injection of the mixture of Zoletil (20 mg/kg) and Xylazine (11 mg/kg). After the anesthetization, abdominal hair was removed by using hair clipper and hair removal cream. Small incision with size of 10 mm was made on skin and peritoneum. Then the left lobe of liver was carefully exposed. The cover glass attached with a silicone rubber heater and mini-probe thermometer was placed on the exteriorized liver to monitor and maintain the temperature of local liver tissue constant at 36 °C during the intravital imaging. Additionally, a commercial homeothermic heating pad (RightTemp Jr., Kent Scientific, USA) was used to maintain the body temperature at 36 °C during the intravital imaging. A wet gauze soaked with warmed saline was placed between the liver and adjacent tissue to reduce motion artifacts. To avoid dehydration of the surface of the exteriorized liver, warmed saline was continuously supplied to the gauze during the imaging. During the intravital imaging, the level of anesthetization was periodically monitored by pinching the toe. When the movement was observed, the half of the initial dose of Zoletil and Xylazine mixture was administered by intramuscular injection. The fs-pulse Ti:Sapphire laser was tuned to a wavelength of 900 nm with 46.3 mW under the objective lens for simultaneous two-photon excitation fluorescence (TPEF) imaging of hepatic LDs and label-free second harmonic generation (SHG) imaging of collagen. Hepatic LDs were fluorescently labeled *in vivo* by intravenous injection of SF44 (120 µl of 1.67 mM; SPARK Biopharma, Korea) at 30 minutes before the imaging. Liver sinusoidal vessels were fluorescently labeled *in vivo* by intravenous injection of anti-CD31 monoclonal antibody conjugates (553370, BD Bioscience). Images were acquired with a high numerical aperture water immersion objection lens (CFI75 Apochromat 25XC W, NA 1.1, Nikon, Japan) providing FOV of 443 × 443 µm with 1024 × 1024 pixels in image and pixel size of 0.433 µm. TPEF and SHG signals were detected through bandpass filters at 565-605nm and 435-455nm, respectively. To perform subcellular quantification of the hepatic LDs accumulation and collagen fibers deposition, z-stack images with thickness of 40 µm with 2 µm interval were obtained. The z-stack images were acquired at more than 10 randomly selected spots in the liver. Each image was obtained by averaging 45 frames acquired at the speed of 15 frames per second (fps) for 3 seconds.

2.4. Imaging analysis and statistical analysis

Acquired z-stack images were converted to 3D-rendered volume images for a quantitative analysis of hepatic LDs and collagen fibers by using commercial image analysis software, IMARIS (Oxford Instruments, UK). Acquisition of all images was performed in same imaging condition with same laser power and objective lens. By using the 'Surface' function of the IMARIS, the volume occupied by hepatic LDs and collagen fibers in the imaging volume were automatically detected and measured. To measure hepatic LDs or collagen fiber volume, we set the voxel size in X, Y and Z axes to match the actual size of the acquired images. Voxel sizes of X and Y can be determined by the field of view of image. The field of view of all images was 443 × 443 µm and the number of pixels of 1024 × 1024 pixels, resulting in the pixel size of 0.433 µm. The setting values of a voxel size in both X and Y axes were set to 0.433 µm. And the setting value of a voxel size in Z axis was set to 2 µm because the z-stack images were obtained with 2 µm interval. After the adjustment of geometrical settings for the voxel, we automatically quantified the volume of hepatic LDs and collagen fibers. Due to differences in the fluorescence signals from hepatic LDs and collagen fibers, we used different parameters in two cases. To create surfaces of LD signals, we selected red color. To distinguish each lipid droplet from neighboring other lipid droplets, we set the Diameter of Largest Sphere and the Surface Area Detailed Level to 3 µm and 0.3 µm, respectively. The manual setting of the low and high threshold was adjusted to precisely detect LD signals with minimal background signal. The setting values of low and high threshold were set to 41 and 226.8, respectively. To create surfaces of collagen fiber, we selected green color

Biomedical Optics EXPRESS

with the same setting values of the Diameter of Largest Sphere and the Surface Area Detailed Level, 2 μm and 0.2 μm, respectively. The values of low and high threshold were set to 25.6 and 205.3, respectively. We validated that when we applied these parameters to all z-stack images obtained from different mice, the surfaces of LD or collagen signals were clearly created. Then, the automatically measured values of hepatic LD or collagen fiber volume and the total imaging volume were exported for quantification analysis. The volumetric ratios occupied by hepatic LDs and collagen were calculated by dividing the total volume of hepatic LDs and collagen fibers

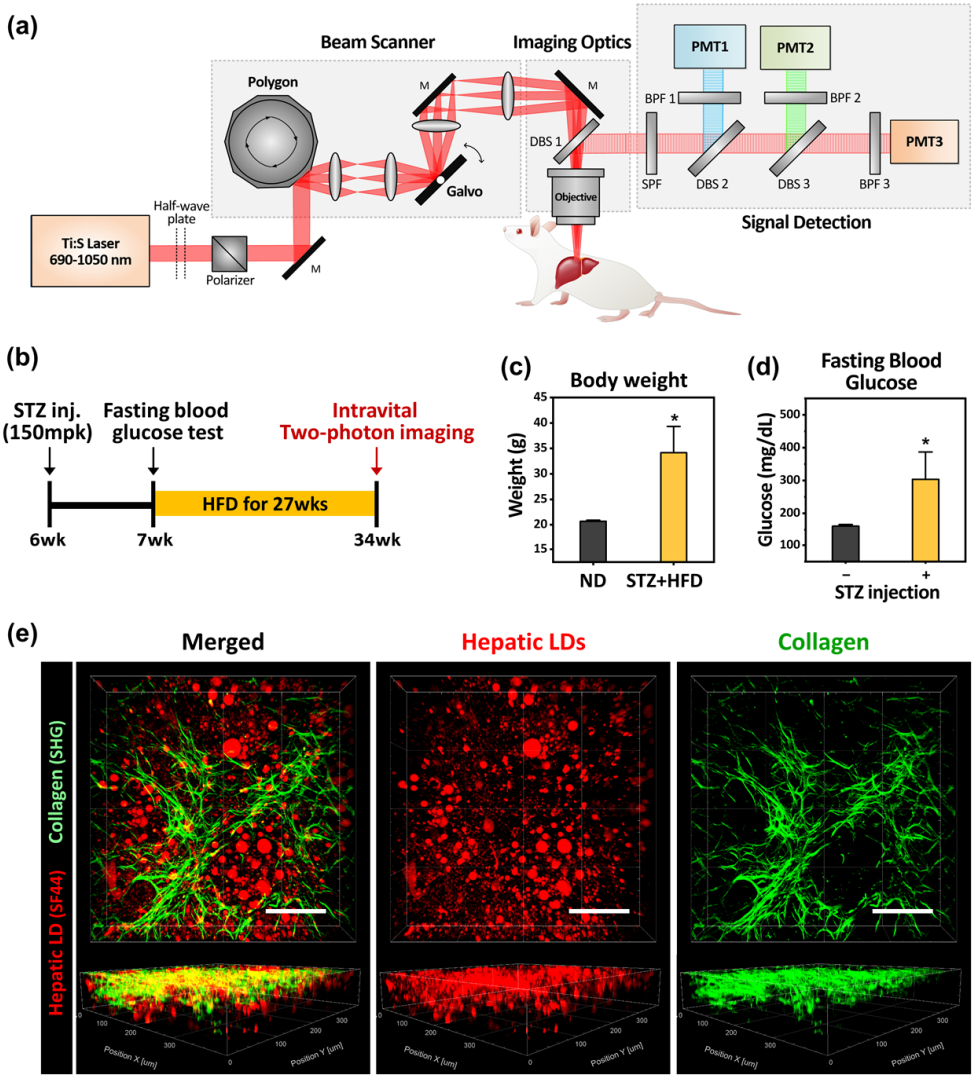

Fig. 1. Intravital two-photon imaging of the liver of diabetic NAFLD mouse model. (a) Schematic of custom-built video-rate laser scanning two-photon microscopy system. (b) Experimental scheme for induction of diabetic mouse model with NAFLD and intravital liver imaging. (c-d) Body weight, fasting blood glucose of STZ-treated high-fat diet fed mouse (STZ + HFD) and normal diet fed mouse (ND). (e) Representative 3-dimensionally reconstructed image of hepatic lipid droplets (LDs, red) and collagen (green). Scale bars, 100μm. Data are presented as mean ± SD of mean. Statistical significance was set at p-value less than 0.05.

Biomedical Optics EXPRESS

with the total imaging volume. The diameter of individual hepatic LDs was measured by using Image J (NIH, USA) [27]. To quantify vessel area and length, sinusoidal microvasculature was automatically identified by using AngioTool (NIH, USA). Statistical analysis was performed by using Origin (OriginLab, USA). Data are presented as mean ± SD. 3 mice were analyzed for each experimental group. Statistical differences were determined by two-tailed unpaired Student's t-test. Statistical significance was set at p-value less than 0.05.

3. Results

To visualize the hepatic lipid droplets and fibrous collagen in the liver *in vivo*, a previously described custom-built laser-scanning two-photon microscopy system was used [20] (Fig. 1(a)). As a diabetic animal model with NAFLD, mice treated with a high dose of streptozotocin (STZ) at 6 weeks of age were subsequently fed a high-fat diet for 27 weeks, manifesting an excessive gain of body weight and elevated level of fasting blood glucose (Fig. 1(b-d)). Using the two-photon

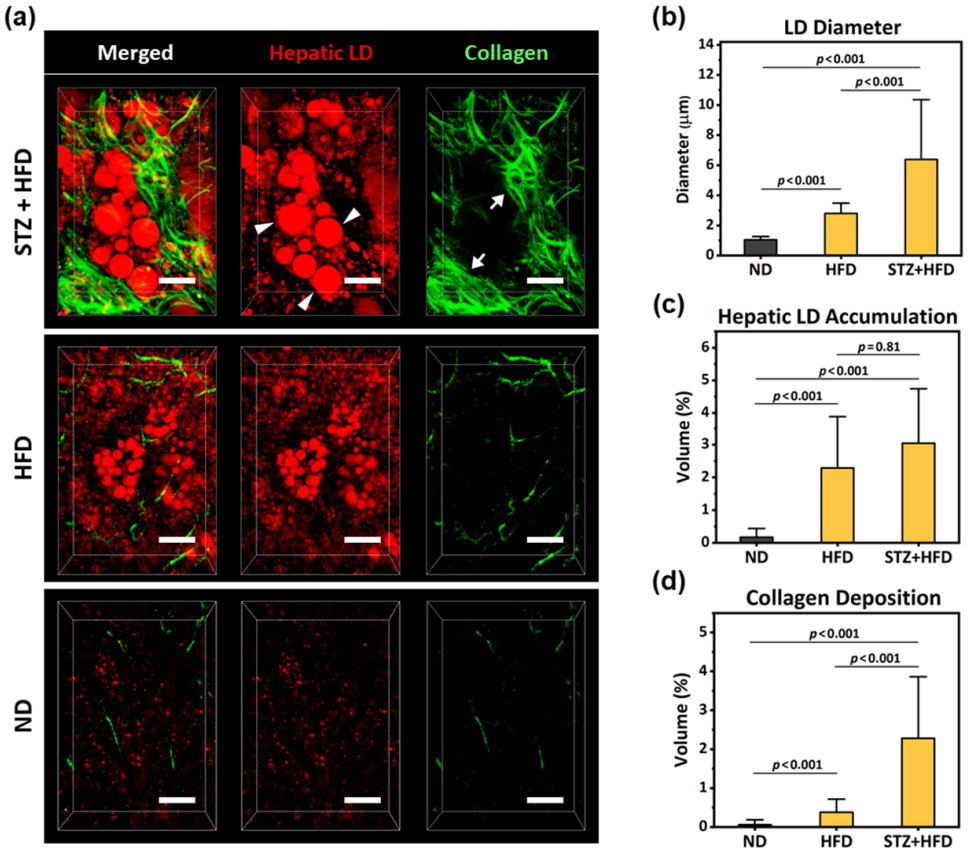

Fig. 2. Subcellular-level intravital two-photon imaging and quantification of hepatic LDs and collagen fiber. (a) Representative magnified 3-dimensionally reconstructed images showing subcellular level features, accumulation of hepatic LDs (red, arrowhead) and perisinusoidal collagen (green, arrow), in the liver of STZ-treated high-fat diet fed mouse (STZ + HFD), only high-fat diet fed mouse (HFD) and normal diet fed mouse (ND). Scale bars, 20 μm. (b-d) Average LD diameter, 3D volumetric proportion occupied by hepatic LD and collagen in the total imaging volume (n=3). Data are presented as mean ± SD of mean. Statistical significance was set at p-value less than 0.05.

Biomedical Optics EXPRESS

intravital microscopy system, a subcellular-level *in vivo* 3D visualization of hepatic LDs in hepatocytes and perisinusoidal collagen in the liver of live anesthetized mouse model for NAFLD with diabetes was successfully achieved (Fig. 1(e)). Accumulation of large spherical-shaped hepatic LDs fluorescently labeled by intravenous injection of lipid droplet specific fluorophore, SF44 [28–30], hepatic steatosis, were clearly imaged *in vivo*. Additionally, significant fibrotic collagen deposition in the liver stroma, liver fibrosis, was successfully visualized by label-free second harmonic generation (SHG) imaging [13]. Notably, the image of hepatic LDs and collagen fibers were simultaneously captured with the single wavelength two-photon excitation at 900nm.

In the magnified 3D rendered images, distinctive subcellular level histopathological features of advanced NAFLD such as accumulation of macrovesicular LDs (Fig. 2(a), arrowheads) in hepatocytes and perisinusoidal deposition of collagen fibers (Fig. 2(a), arrows) were clearly identifiable. Furthermore, we could precisely quantify the mean diameter of hepatic LDs and volumetric proportions occupied by hepatic LDs and collagen fibers in the total imaging volume (Fig. 2(b-d)) (mouse, n=3). In the liver of STZ-treated HFD fed mice, greatly enlarged hepatic LDs with diameter around 6 μm (average diameter = 6.38 ± 2.65 μm) were observed. The volumetric proportion occupied by hepatic LDs in the total imaging volume was significantly increased to 3.05% more than 10 times in comparison to that of the normal diet, 0.17%, suggesting severe steatosis. The volumetric ratio occupied by collagen fiber was significantly elevated to 2.28% more than 10 times in comparison to that of the normal diet, 0.06%, indicating fibrosis. Interestingly, in the liver of only HFD fed mice without STZ treatment for the same period of 27 weeks, the similar level of volumetric proportion increases in LDs (2.29%) but with much smaller diameter (mean diameter = 2.80 ± 0.45 μm) was observed, suggesting slightly lesser degree of

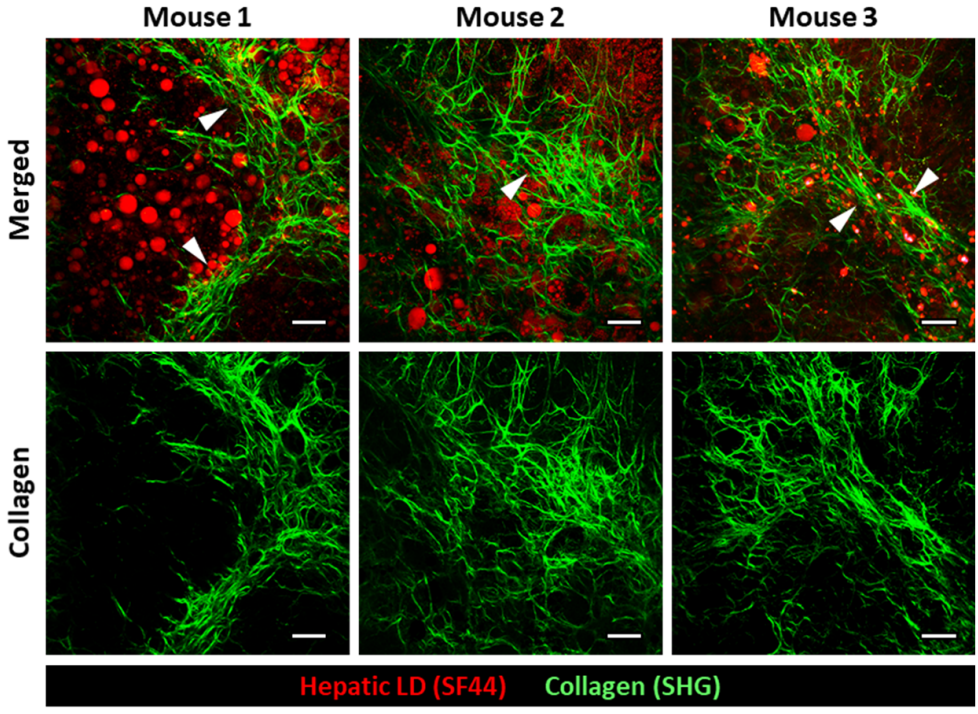

Fig. 3. Fibrous septa formation in the liver of diabetic NAFLD mouse model. Representative images showing interlobular collagen fiber septa formation (arrowhead) in all of the STZ-treated HFD fed mice (n=3). Scale bars, 50 μm.

Biomedical Optics EXPRESS

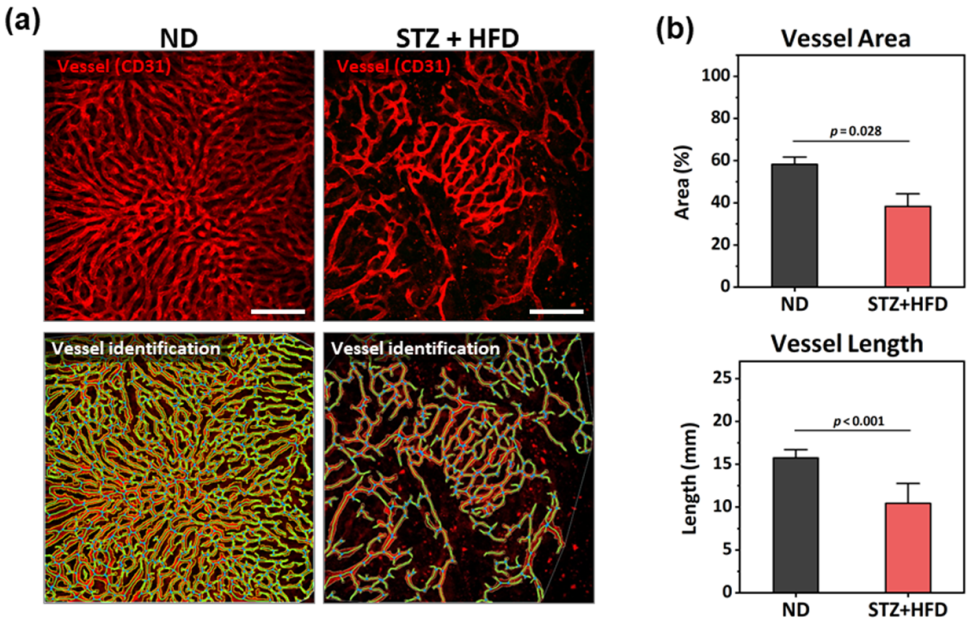

Fig. 4. Structural distortion of sinusoidal microvasculature in the liver of diabetic NAFLD mouse model. (a) Representative images of sinusoidal vessels (red) and automatic identification of vessels in the liver STZ-treated high-fat diet fed mouse (STZ + HFD) and normal diet fed mouse (ND) (n=3). Scale bars, 100 μm. (b) Quantification of vessel area and length. Data are presented as mean ± SE of mean. Statistical significance was set at p-value less than 0.05.

steatosis. Furthermore, only marginal increase in the volumetric proportion of collagen fiber (0.38%) was observed, suggesting no fibrosis development. Finally, in the liver of mice fed a normal diet (ND), only a few very small LDs with diameter smaller than 1 μm and minimal level of stromal collagen fiber were observed. Additionally, in human NAFLD patient, the pathological hallmark of the advanced stage of fibrosis is the formation of fibrous septa composed of parallel arrays of collagen fibers in the liver. Notably, in all of the STZ-treated HFD fed mice (n=3), septa formation with thick and parallel arrays of collagen fibers was clearly visualized by SHG imaging (Fig. 3).

Additionally, the liver sinusoidal microvasculature was successfully visualized *in vivo* by fluorescent labeling of endothelial cells with intravenous injection of anti-CD31 antibody conjugates (Fig. 4). Compared to the uniformly distributed dense sinusoidal vessels in the liver of mice fed a normal diet (ND), severe distortions such as rarefaction and dilation in the sinusoidal vessels were clearly observed in the liver of STZ-treated HFD fed mice. Both of vessel area and length were significantly decreased more than 30% in comparison to those values in the ND fed mice.

4. Discussion

NAFLD represents the liver manifestation of metabolic syndrome and strongly associated with obesity and type 2 diabetes [4,5]. Insulin resistance is the common pathophysiologic mechanism of these conditions [30–32]. However, the effect of insulin deficiency on this ectopic fat accumulating condition is not fully uncovered yet. Our result of significantly increased hepatic LD diameter and perisinusoidal collagen deposition by STZ treatment in HFD-fed mice suggests insulin

Biomedical Optics EXPRESS

deficiency can be a strong driving factor aggravating NAFLD (Fig. 2). In addition to common retrospective clinical studies, a prospective study utilizing a preclinical animal model combined with direct longitudinal intravital imaging for subcellular-level visualization of pathophysiological features would be valuable approach to improve our currently limited understanding about the underlying mechanism in the development of NAFLD associated with insulin deficiency other than resistance. Several intravital two-photon imaging studies have been successfully performed with preclinical animal model to investigate dynamic pathological phenomenon such as hepatic lymphocyte migration with experimental liver injury or impaired hepatobiliary metabolism with liver fibrosis [33,34]. Utilization of surgically implantable abdominal imaging chamber [35–38] can facilitate an effective long-term longitudinal observation in the same area of liver developing NAFLD with reduced number of required animals. Notably, recent advances of various optical imaging system with different modalities can further expand the scope of obtainable information [38]. Label-free imaging modalities including coherent anti-Stokes Raman scattering (CARS) microscopy [39], third-harmonics generation microscopy [40], autofluorescence three-photon excitation microscopy [41] and two-photon autofluorescence lifetime microscopy [42–44] can be used to visualize lipids and metabolism in biological tissues with minimal risk of interfering liver physiology potentially caused by exogenous fluorophore injection for the staining of cellular components. Despite a caveat, the utilization of exogenous fluorophore to label LDs *in vivo* can readily achieve high sensitivity and high signal to background ratio in the visualization of hepatic LDs. Furthermore, the SF44 used in this work to label LDs was rapidly washed out from the liver within 4 hours with negligible toxicity [21]. Other label-free imaging techniques including optical coherence tomography angiography (OCTA) [45–47], ultrasonography combined with photoacoustic tomography (PAT) imaging [48] and magnetic resonance (MR) imaging [9,49] can provide additional information about vascular functions, lipid accumulation and degree of fibrosis in the liver in a minimally or noninvasive manner although the imaging resolution is relatively low not enough for cellular-level analysis.

In this study, we successfully achieved a subcellular-level *in vivo* visualization of hepatic microenvironment in the liver of anesthetized streptozotocin (STZ)-treated diabetic mice fed HFD for 27 weeks. Extensive lipid accumulation in hepatocytes accompanied with fibrotic collagen deposition in insulin deficient condition with HFD was observed by intravenously injected LD-specific fluorophore, SF44, and second harmonic generation signal, respectively. Pathological features of hepatocellular steatosis and fibrosis such as accumulation of macrovesicular LD in hepatocyte, perisinusoidal collagen deposition, septa formation and severely distorted sinusoidal vasculature were clearly imaged *in vivo* and quantified with 3-dimensional Z-stack imaging data. The established intravital two-photon imaging method to visualize and quantify subcellular-level LDs, collagen, and vasculature in the liver of live animal model can be a valuable tool to analyze a highly complex pathophysiology of NAFLD with diabetes mellitus and to assess the efficacy of novel treatment strategies to intervene the progression of NAFLD in preclinical studies.

Funding. National Research Foundation of Korea (2020R1A2C3005694).

Acknowledgements. The authors would like to thank Jieun Choi, and Lucia Stephani Edwina for their technical assistances.

Disclosures. The authors declare that there are no conflicts of interest related to this article.

Data availability. Data underlying the results presented in this paper are not publicly available at this time but may be obtained from the authors upon resonable request.

References

1. S. L. Friedman, B. A. Neuschwander-Tetri, M. Rinella, and A. J. Sanyal, "Mechanisms of NAFLD development and therapeutic strategies," Nat. Med. **24**(7), 908–922 (2018).
2. Z. M. Younossi, A. B. Koenig, D. Abdelatif, Y. Fazel, L. Henry, and M. Wymer, "Global epidemiology of nonalcoholic fatty liver disease—Meta-analytic assessment of prevalence, incidence, and outcomes," Hepatology **64**(1), 73–84 (2016).

Biomedical Optics EXPRESS

3. E. Fabbrini, S. Sullivan, and S. Klein, "Obesity and nonalcoholic fatty liver disease: Biochemical, metabolic, and clinical implications," Hepatology **51**(2), 679–689 (2010).
4. G. Targher, L. Bertolini, R. Padovani, S. Rodella, R. Tessari, L. Zenari, C. Day, and G. Arcaro, "Prevalence of nonalcoholic fatty liver disease and its association with cardiovascular disease among type 2 diabetic patients," Diabetes Care **30**(5), 1212–1218 (2007).
5. Q. M. Anstee, G. Targher, and C. P. Day, "Progression of NAFLD to diabetes mellitus, cardiovascular disease or cirrhosis," Nat. Rev. Gastroenterol. Hepatol. **10**(6), 330–344 (2013).
6. P. Burra, C. Becchetti, and G. Germani, "NAFLD and liver transplantation: disease burden, current management and future challenges," JHEP Rep. **2**(6), 100192 (2020).
7. I. Nalbantoglu and E. M. Brunt, "Role of liver biopsy in nonalcoholic fatty liver disease," World J. Gastroenterol. **20**(27), 9026–9037 (2014).
8. E. M. Brunt, D. E. Kleiner, L. A. Wilson, P. Belt, and B. A. Neuschwander-Tetri, "Nonalcoholic fatty liver disease (NAFLD) activity score and the histopathologic diagnosis in NAFLD: Distinct clinicopathologic meanings," Hepatology **53**(3), 810–820 (2011).
9. G. Marchesini, C. P. Day, J. F. Dufour, A. Canbay, V. Nobili, V. Ratziu, H. Tilg, M. Roden, A. Gastaldelli, H. Yki-Jarvinen, F. Schick, R. Vettor, G. Fruhbeck, and L. Mathus-Vliegen, "EASL-EASD-EASO Clinical Practice Guidelines for the management of non-alcoholic fatty liver disease," J. Hepatol. **64**(6), 1388–1402 (2016).
10. V. W. S. Wong, L. A. Adams, V. de Lédinghen, G. L. H. Wong, and S. Sookoian, "Noninvasive biomarkers in NAFLD and NASH: current progress and future promise," Nat. Rev. Gastroenterol. Hepatol. **15**(8), 461–478 (2018).
11. L. Castera, M. Friedrich-Rust, and R. Loomba, "Noninvasive assessment of liver disease in patients with nonalcoholic fatty liver disease," Gastroenterology **156**(5), 1264–1281.e4 (2019).
12. C. A. Thorling, D. Crawford, F. J. Burczynski, X. Liu, I. Liau, and M. S. Roberts, "Multiphoton microscopy in defining liver function," J. Biomed. Opt. **19**(9), 090901 (2014).
13. W. R. Zipfel, R. M. Williams, and W. W. Webb, "Nonlinear magic: multiphoton microscopy in the biosciences," Nat. Biotechnol. **21**(11), 1369–1377 (2003).
14. W. Sun, S. Chang, D. C. S. Tai, N. Tan, G. Xiao, H. Tang, and H. Yu, "Nonlinear optical microscopy: use of second harmonic generation and two-photon microscopy for automated quantitative liver fibrosis studies," J. Biomed. Opt. **13**(6), 064010 (2008).
15. J. K. C. Lau, X. Zhang, and J. Yu, "Animal models of non-alcoholic fatty liver disease: current perspectives and recent advances," J. Pathol. **241**(1), 36–44 (2017).
16. R. Kirsch, V. Clarkson, E. G. Shephard, D. A. Marais, M. A. Jaffer, V. E. Woodburne, R. E. Kirsch, and P. d. l. M. Hall, "Rodent nutritional model of non-alcoholic steatohepatitis: species, strain and sex difference studies," J. Gastroenterol. Hepatol. **18**(11), 1272–1282 (2003).
17. M. Ito, J. Suzuki, S. Tsujioka, M. Sasaki, A. Gomori, T. Shirakura, H. Hirose, M. Ito, A. Ishihara, H. Iwaasa, and A. Kanatani, "Longitudinal analysis of murine steatohepatitis model induced by chronic exposure to high-fat diet," Hepatol. Res. **37**(1), 50–57 (2007).
18. Y. Takahashi and T. Fukusato, "Histopathology of nonalcoholic fatty liver disease/nonalcoholic steatohepatitis," World J. Gastroenterol. **20**(42), 15539–15548 (2014).
19. S. Caldwell, Y. Ikura, D. Dias, K. Isomoto, A. Yabu, C. Moskaluk, P. Pramoonjago, W. Simmons, H. Scruggs, N. Rosenbaum, T. Wilkinson, P. Toms, C. K. Argo, A. M. S. Al-, and J. A. Redick, "Hepatocellular ballooning in NASH," J. Hepatol. **53**(4), 719–723 (2010).
20. J. Moon, "Intravital two-photon imaging of dynamic alteration of hepatic lipid droplets in fasted and refed state," J. Lipid and Atherosclerosis **10**(3), 313 (2021).
21. J. Moon, E. Kong, J. Lee, J. Jung, E. Kim, S. B. Park, and P. Kim, "Intravital longitudinal imaging of hepatic lipid droplet accumulation in a murine model for nonalcoholic fatty liver disease," Biomed. Opt. Express **11**(9), 5132 (2020).
22. J. Lee, E. Kong, S. Hong, J. Moon, and P. Kim, "In vivo longitudinal visualization of the brain neuroinflammatory response at the cellular level in LysM-GFP mice induced by 3-nitropropionic acid," Biomed. Opt. Express **11**(8), 4835 (2020).
23. I. Park, M. Kim, K. Choe, E. Song, H. Seo, Y. Hwang, J. Ahn, S. Lee, J. H. Lee, Y. H. Jo, K. Kim, G. Y. Koh, and P. Kim, "Neutrophils disturb pulmonary microcirculation in sepsis-induced acute lung injury," Eur. Respir. J. **53**(3), 1800786 (2019).
24. I. Park, K. Choe, H. Seo, Y. Hwang, E. Song, J. Ahn, Y. Hwan Jo, and P. Kim, "Intravital imaging of a pulmonary endothelial surface layer in a murine sepsis model," Biomed. Opt. Express **9**(5), 2383 (2018).
25. Y. Hwang, H. Yoon, K. Choe, J. Ahn, J. H. Jung, J.-H. Park, and P. Kim, "In vivo cellular-level real-time pharmacokinetic imaging of free-form and liposomal indocyanine green in liver," Biomed. Opt. Express **8**(10), 4706 (2017).
26. S. Ahn, K. Choe, S. Lee, K. Kim, E. Song, H. Seo, I. Kim, and P. Kim, "Intravital longitudinal wide-area imaging of dynamic bone marrow engraftment and multilineage differentiation through nuclear-cytoplasmic labeling," PLoS One **12**(11), e0187660 (2017).
27. E. Zudaire, L. Gambardella, C. Kurcz, and S. Vermeren, "A computational tool for quantitative analysis of vascular networks," PLoS One **6**(11), e27385 (2011).

Biomedical Optics EXPRESS

28. E. Kim, Y. Lee, S. Lee, and S. B. Park, "Discovery, understanding, and bioapplication of organic fluorophore: a case study with an indolizine-based novel fluorophore, seoul-fluor," Acc. Chem. Res. **48**(3), 538–547 (2015).
29. E. Kim, S. Lee, and S. B. Park, "A Seoul-Fluor-based bioprobe for lipid droplets and its application in image-based high throughput screening," Chem. Commun. **48**(17), 2331 (2012).
30. A. Seppälä-Lindroos, S. Vehkavaara, A. M. Häkkinen, T. Goto, J. Westerbacka, A. Sovijärvi, J. Halavaara, and H. Yki-Järvinen, "Fat accumulation in the liver is associated with defects in insulin suppression of glucose production and serum free fatty acids independent of obesity in normal men," J. Clinical Endocrinology and Metabolism **87**(7), 3023–3028 (2002).
31. V. T. Samuel, Z. X. Liu, X. Qu, B. D. Elder, S. Bilz, D. Befroy, A. J. Romanelli, and G. I. Shulman, "Mechanism of hepatic insulin resistance in non-alcoholic fatty liver disease," J. Biological Chem. **279**(31), 32345–32353 (2004).
32. T. Jelenik, K. Kaul, G. Séquaris, U. Flögel, E. Phielix, J. Kotzka, B. Knebel, P. Fahlbusch, T. Hörbelt, S. Lehr, A. L. Reinbeck, D. Müller-Wieland, I. Esposito, G. I. Shulman, J. Szendroedi, and M. Roden, "Mechanisms of insulin resistance in primary and secondary nonalcoholic fatty liver," Diabetes **66**(8), 2241–2253 (2017).
33. A. Wehr, C. Baeck, F. Heymann, P. M. Niemietz, L. Hammerich, C. Martin, H. W. Zimmermann, O. Pack, N. Gassler, K. Hittatiya, A. Ludwig, T. Luedde, C. Trautwein, and F. Tacke, "Chemokine receptor CXCR6-dependent hepatic NK T cell accumulation promotes inflammation and liver fibrosis," The J. Immunology **190**(10), 5226–5236 (2013).
34. C. J. Lin, S. L. Lee, W. H. Wang, V. A. Hovhannisyan, Y. de Huang, H. S. Lee, and C. Y. Dong, "Multiphoton dynamic imaging of the effect of chronic hepatic diseases on hepatobiliary metabolism in vivo," J. Biophotonics **11**(9), e201700338 (2018).
35. R. Laila, E. J. A. Steller, E. Beerling, C. J. M. Loomans, Z. Anoek, G. Carmen, V. Nienke, S. Daniëlle, L. van Gurp, R. Schäfer, D. A. Raats, A. de Graaff, T. N. Schumacher, E. J. P. de Koning, I. H. Borel Rinkes, O. Kranenburg, and J. van Rheenen, "Intravital microscopy through an abdominal imaging window reveals a pre-micrometastasis stage during liver metastasis," Sci. Transl. Med. **4**(158), 145–158 (2012).
36. L. Ritsma, E. J. A. Steller, S. I. J. Ellenbroek, O. Kranenburg, I. H. M. Borel Rinkes, and J. van Rheenen, "Surgical implantation of an abdominal imaging window for intravital microscopy," Nat. Protocols **8**(3), 583–594 (2013).
37. D. Deng, B. Dai, J. Wei, X. Yuan, X. Yang, S. Qi, and Z. Zhang, "A drawer-type abdominal window with an acrylic/resin coverslip enables long-term intravital fluorescence/photoacoustic imaging of the liver," Nanophotonics **10**(12), 3369–3381 (2021).
38. E. Chung and A. Vitkin, "Photon mayhem: new directions in diagnostic and therapeutic photomedicine," Biomed. Eng. Lett. **9**(3), 275–277 (2019).
39. J. Lin, F. Lu, W. Zheng, S. Xu, D. Tai, H. Yu, and Z. Huang, "Assessment of liver steatosis and fibrosis in rats using integrated coherent anti-Stokes Raman scattering and multiphoton imaging technique," J. Biomed. Opt. **16**(11), 116024 (2011).
40. D. Débarre, W. Supatto, A.-M. Pena, A. Fabre, T. Tordjmann, L. Combettes, M.-C. Schanne-Klein, and E. Beaurepaire, "Imaging lipid bodies in cells and tissues using third-harmonic generation microscopy," Nat. Methods **3**(1), 47–53 (2006).
41. S. You, H. Tu, E. J. Chaney, Y. Sun, Y. Zhao, A. J. Bower, Y. Z. Liu, M. Marjanovic, S. Sinha, Y. Pu, and S. A. Boppart, "Intravital imaging by simultaneous label-free autofluorescence-multiharmonic microscopy," Nat. Commun. **9**(1), 2125 (2018).
42. A. J. Bower, J. Li, E. J. Chaney, M. Marjanovic, D. R. Spillman, and S. A. Boppart, "High-speed imaging of transient metabolic dynamics using two-photon fluorescence lifetime imaging microscopy," Optica **5**(10), 1290 (2018).
43. Y. Zhang, I. H. Guldner, E. L. Nichols, D. Benirschke, C. J. Smith, S. Zhang, and S. S. Howard, "Instant FLIM enables 4D in vivo lifetime imaging of intact and injured zebrafish and mouse brains," Optica **8**(6), 885 (2021).
44. H. Ranawat, S. Pal, and N. Mazumder, "Recent trends in two-photon auto-fluorescence lifetime imaging (2P-FLIM) and its biomedical applications," Biomed. Eng. Lett. **9**(3), 293–310 (2019).
45. J. Joo, T. S. Kim, B. J. Vakoc, and W.-Y. Oh, "Robust and easy-to-operate stretched-pulse mode-locked wavelength-swept laser with an all-polarization-maintaining fiber cavity for 10 MHz A-line rate optical coherence tomography," Opt. Lett. **46**(16), 3857 (2021).
46. S. Wei and J. U. Kang, "Optical flow optical coherence tomography for determining accurate velocity fields," Opt. Express **28**(17), 25502 (2020).
47. W. J. Choi, "Optical coherence tomography angiography in preclinical neuroimaging," Biomed. Eng. Lett. **9**(3), 311–325 (2019).
48. G. S. Sangha, E. H. Phillips, and C. J. Goergen, "In vivo photoacoustic lipid imaging in mice using the second near-infrared window," Biomed. Opt. Express **8**(2), 736 (2017).
49. A. Tang, J. Tan, M. Sun, G. Hamilton, M. Bydder, T. Wolfson, A. C. Gamst, M. Middleton, E. M. Brunt, R. Loomba, J. E. Lavine, J. B. Schwimmer, and C. B. Sirlin, "Nonalcoholic fatty liver disease: MR imaging of liver proton density fat fraction to assess hepatic steatosis," Radiology **267**(2), 422–431 (2013).